

Combined Monte Carlo and k-Wave Simulations for Reconstruction of Blood Oxygen Saturation in Optoacoustics: A Pilot Study

Valeriya Perekatova*, Daria Kurakina, Aleksandr Khilov, and Mikhail Kirillin

Institute of Applied Physics RAS, 46 Ul'yanov str., Nizhny Novgorod 603950, Russia

* e-mail: valeriyaperekatova@gmail.com

Abstract. Optoacoustic (OA) imaging of biological tissues is a modern technique allowing for three-dimensional blood oxygen saturation mapping based on OA spectroscopy data. Since biological tissues are optically inhomogeneous and the spatial distribution of optical parameters within a biological tissue is a priori unknown, Monte Carlo simulation technique is traditionally used to estimate the distribution of probing illumination within tissues in quantitative OA reconstruction. Currently, machine learning techniques are actively employed for reconstructing 3D distribution of blood oxygen saturation or estimating optical properties of biological tissues based on training datasets. In this paper, systemic calculations of synthetic OA images of a medium with embedded vessel-like structures were performed to create a training dataset for machine learning employing combined application of the Monte Carlo technique for direct solution of optical problem and difference-space pseudo-spectral approach implemented through k-Wave Toolbox calculations for the acoustical part. The calculations were performed for probing wavelengths of 532 nm, 658 nm and 1064 nm, which are commonly employed in spectral OA imaging. Simulated OA data for different orientation, diameter and embedding depth of blood vessels allows analyzing the effect of these parameters on the formation of OA image and the reconstruction of blood oxygen saturation. The ratio of OA signals corresponding to probing wavelengths of 658 nm and 1064 nm was employed for simple reconstruction of blood oxygen saturation *in silico* for different vessel geometries with the precision of < 3–15% for the most of blood vessels diameters and embedding depths and the range of blood oxygen saturation values ≥ 0.8 . The obtained set of synthetic OA data has high potential as a training set for employment in machine learning techniques aiming at mapping blood oxygenation based on spectral OA data. © 2022 Journal of Biomedical Photonics & Engineering.

Keywords: optoacoustic imaging; Monte Carlo modeling; k-Wave modeling; blood oxygen saturation mapping.

Paper #3562 received 10 Nov 2022; revised manuscript received 7 Dec 2022; accepted for publication 12 Dec 2022; published online 24 Dec 2022. doi: [10.18287/JBPE22.08.040511](https://doi.org/10.18287/JBPE22.08.040511).

1 Introduction

Blood oxygen saturation (blood oxygenation level, StO_2) is an important physiological indicator actively

used in monitoring of functional parameters in biomedical studies, such as the evaluation of chemo- and radiation therapy impact on tumor tissue [1, 2], monitoring of wounds healing [3], or estimation of

tissue reaction to photodynamic therapy [4]. In this regard, the development of a non-invasive visualization technique capable of providing fast *in vivo* three-dimensional mapping of blood oxygenation level is of high importance. Optical imaging techniques [5, 6] benefit from both non-invasiveness and high sensitivity to blood oxygenation owing to significant difference in absorption spectra of oxy- and deoxyhemoglobin in optical spectral range. Traditionally, blood oxygenation level is estimated with diffuse optical spectroscopy (DOS) [2, 7, 8] based on the registration of the spectra of the probing radiation passed through the biological tissue and the subsequent reconstruction of the medium absorption spectra from the measurement data [9, 10]. This approach, however, provides with the estimation of blood oxygenation value averaged over a particular measurement volume within biological tissue. Blood saturation mapping provides a more detailed information regarding tissue oxygenation and could be performed using diffuse optical tomography (DOT) [11, 12], however, at the expense of spatial resolution of order of 0.5 cm. Nevertheless, the estimation of local oxygenation at tissue layer level in certain blood vessels may be required, for example, for the studies of hemodynamics [13, 14]. Optoacoustic (OA) imaging [15–19] is a modern hybrid imaging technique with high potential in saturation mapping [20] owing to high spatial resolution combined with increased probing depth compared to purely optical modalities.

This technique is often employed for superficial vasculature mapping providing resolution down to tens of microns and imaging depth of several centimeters, which allows obtaining *in vivo* morphological and functional information on the vascular bed of biological tissue. The contrast of OA images is determined by the difference in the absorption coefficient of blood and surrounding components of the biological tissue revealing high potential for *in vivo* angiography. Since the optical absorption spectra of oxy- and deoxyhemoglobin differ significantly, spectral separation of these chromophores can be performed based on OA spectroscopy data with consequent determination of blood oxygen saturation [20, 21].

However, the local pressure increment that occurs in the medium due to absorption of pulsed laser radiation by optical inhomogeneities is proportional to the local optical absorption coefficient and the fluence of the probing optical radiation at a given point in the medium. Since biological tissues are optically inhomogeneous and the distribution of optical parameters of a biological tissue is a priori unknown, Monte Carlo simulation technique is traditionally used to estimate the distribution of probing illumination within tissues in quantitative OA imaging [22]. Reconstruction of 3D distribution of functional tissue parameters from OA data benefits from current development of machine learning (ML) techniques. Currently, ML methods (for example, artificial neural networks) are actively employed for reconstructing maps of blood oxygen saturation distribution or estimating

optical properties of biological tissues based on training OA datasets [23–25]. Some of approaches using neural networks estimate oxygenation from single-pixel pressure spectra [26, 27]. Employment of convolutional neural networks allows to process the spectra of entire 2D (3D) images utilizing spatial and spectral information at the same time [28–31]. Due to the lack of experimental training data with a priori known saturation distribution within tissue, synthetic data are commonly used for training the neural network and proof-of-concept verification [23, 24]. In order to accumulate synthetic datasets for training algorithms, it is essential to realistically model the physical processes of optoacoustic imaging.

In this paper, to create a training sample dataset, systemic calculations of OA images were performed employing sequential application of the Monte Carlo method for direct solution of optical problem and k-space pseudo-spectral approach for acoustics. A simple approach to blood oxygen saturation reconstruction based on the revealed monotonous dependence of registered OA signal ratio for probing wavelengths of 658 nm and 1064 nm was proposed and tested at the synthetic data. Obtained results indicated high potential of the developed approach to OA images simulations for further development of ML-based algorithms of the estimation of blood oxygen saturation.

2 Materials and Methods

2.1 Monte Carlo Modeling

Traditional Monte Carlo (MC) technique for light transport studies is based on modeling of a large number of random photon trajectories in turbid media with following statistical analysis of the collected data [32]. In this work previously developed platform for three-dimensional MC modeling of light propagation in biological tissues [22, 33, 34] was customized by implementing elongated absorbers mimicking different vessels filled with blood within biotissue. It was employed for the generation of the maps of the absorbed light dose distribution at probing wavelength λ_{ex} $H(x, y, z, \lambda_{ex})$ in a flat tissue-like homogenous medium containing cylinders mimicking blood vessels of different diameters, embedding depths and orientations corresponding to typical morphological parameters.

The full size of a tissue sample considered in simulations was $20 \times 20 \times 10 \text{ mm}^3$. The light source was considered to be a plane wave illuminating the sample from the top. A total of 10^7 photons were launched into the medium perpendicular to the tissue surface and used to calculate $H(x, y, z, \lambda_{ex})$ for each of three probing wavelengths: $\lambda_{ex} = 532, 658, \text{ and } 1064 \text{ nm}$. The wavelengths of 532 nm and 1064 nm are the wavelengths commonly employed for OA imaging [35], while the pair of 658 nm and 1064 nm is optimal for more precise estimation of blood oxygen saturation [36]. The refractive index was set equal to 1.38 for blood vessels as well as for background tissue.

Table 1 Ranges of the optical properties used in Monte Carlo simulations.

Wavelength, nm	Human skin <i>in vivo</i>			Blood (StO ₂ varies from 0.1 to 1)		
	μ_a , mm ⁻¹	μ_s , mm ⁻¹	g	μ_a , mm ⁻¹	μ_s , mm ⁻¹	g
532	0.39	13.29	0.67	19.04–22.48	92.07–98.65	0.989–0.988
658	0.06	9.96	0.67	1.51–0.15	82.94–92.74	0.986–0.985
1064	0.04	5.9	0.67	0.23–0.45	42.19–47.75	0.973–0.972

Table 2 Parameters of the simulated medium and ultrasonic detector for acoustic simulations.

Biotissue				Detector		
Acoustic attenuation, mm ⁻¹ MHz ⁻¹	Time scale, ns	Grid element size, mm	Volume size, mm ³	Numerical aperture	Maximum supported frequency, MHz	Radius, mm
0.01	10	0.05	17.8 × 7.8 × 12.05	0.71	15	6

Fig. 1 Three examples of side views of blood vessels configuration: a) $0.1 \text{ mm} \leq z_0 \leq 0.7 \text{ mm}$ and $0.1 \text{ mm} \leq d \leq 0.25 \text{ mm}$, b) $0.9 \text{ mm} \leq z_0 \leq 1.5 \text{ mm}$ and $0.3 \text{ mm} \leq d \leq 0.45 \text{ mm}$, c) $0.5 \text{ mm} \leq z_0 \leq 1.1 \text{ mm}$ and $0.75 \text{ mm} \leq d \leq 0.9 \text{ mm}$.

Blood oxygen saturation in blood vessels was varied from 0.1 to 1 with the step of 0.1, resulted in different values of the blood optical properties calculated based on absorption and scattering spectra for oxygenated and deoxygenated whole blood taken from [37]. Optical properties for the background tissue were taken from paper [38] for human skin *in vivo*. All the values of optical properties at corresponding wavelengths are shown in Table 1.

2.2 k-Wave Modeling of OA Images

Modeling of OA images of biotissue based on MC-calculated absorption map $H(x, y, z, \lambda_{ex})$ was performed using the k-Wave Toolbox [39], which is a standard for acoustic calculations. The toolbox implements a k-spatial pseudo-spectral method for solving first-order acoustic equations for homogeneous and inhomogeneous media. The employed toolbox can take into account arbitrary distribution of inhomogeneities and acoustic absorption. Monte Carlo simulated maps of the absorbed light dose $H(x, y, z, \lambda_{ex})$ were employed as distributed sources of ultrasonic waves with initial pressure distribution

$$p_0(x, y, z, \lambda_{ex}) = G \cdot H(x, y, z, \lambda_{ex}), \quad (1)$$

where G is the Grüneisen parameter.

The k-Wave modeling of OA microscopy images was implemented in three-dimensional geometry by the solution of the forward acoustic problem for each detector position in XZ-plane. The ultrasonic detector was supposed to be a spherically focused antenna with the parameters close to those for real detector employed in an OA microscope [40–42]. The acoustic properties, grid size and parameters of the biotissue and the ultrasonic detector are shown in Table 2. After k-Wave modeling, each OA microscopy B-scan was processed with the reconstruction algorithm described in paper [43].

Both MC modeling and k-Wave simulations were performed with the employment of workstation equipped with 64-core CPU AMD Ryzen Threadripper 3990X with frequency of 2.9 GHz with 256 Gb RAM onboard.

2.3 Building Synthetic Dataset for Saturation Reconstruction

Numerical simulations were performed for two different geometry configurations of blood vessels distribution. The first one was a simplified model of skin (Fig. 1), containing four blood vessels with parallel axes with different diameters d and embedding depths z_0 .

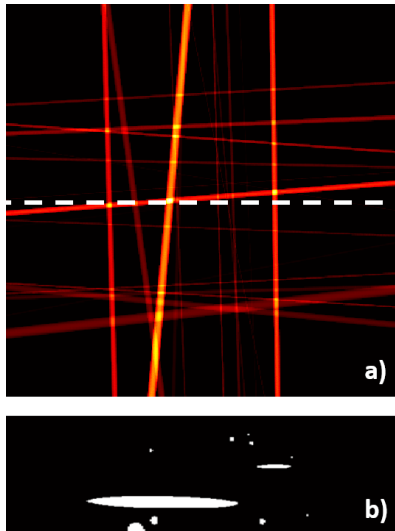


Fig. 2 Complex configuration of vessel net for MC modeling with randomly distributed blood vessels: (a) enface schematic (top view, XY-plane) of vessels orientation (color encodes number of pixels belonging to vessels in corresponding projection); (b) 2D projection (side view, XZ-plane) of blood vessels corresponding to the projection marked with dashed line in Fig. (a).

Fig. 1 shows side views of three examples of such skin models: $0.1 \text{ mm} \leq z_0 \leq 0.7 \text{ mm}$ and $0.1 \text{ mm} \leq d \leq 0.25 \text{ mm}$ (Config 1), $0.9 \text{ mm} \leq z_0 \leq 1.5 \text{ mm}$ and $0.3 \text{ mm} \leq d \leq 0.45 \text{ mm}$ (Config 2), $0.5 \text{ mm} \leq z_0 \leq 1.1 \text{ mm}$ and $0.75 \text{ mm} \leq d \leq 0.9 \text{ mm}$ (Config 3). The total number of combinations of parameters considered in simulations amounted 200, which covered ten different embedding depths z_0 from 0.1 to 1.9 mm and twenty different diameters d from 0.05 to 1 mm. One configuration contained 4 vessels with different parameters resulting in 50 different configurations. Employment of this geometry aims at creating a training dataset that cover the entire range of possible morphological parameters of superficial blood vessels. For all the combinations, ten different values of blood oxygen saturation varying from 0.1 to 1 were considered. Thus, the total number of calculated maps of

$H(x, y, z)$ for different 50 geometries, 3 probing wavelengths and 10 oxygenation values amounted 1500.

Fig. 3 shows the schematic of spherically focused ultrasound detector and initial pressure distribution obtained by MC modeling in projection to XZ-plane for vessel orientation configurations from Fig. 1c and Fig. 2b.

Based on simulated optoacoustic images, a training dataset was created for the implementation of reconstruction methods aiming at the estimation of local blood oxygenation level with a voxel-by-voxel resolution.

2.4 Estimation of Blood Oxygen Saturation

For considered probing wavelengths, the ratios of OA signals $p(x, y, z, \lambda_{ex})$ in central cross-sections ($y = 0$) at different wavelengths $\left(\frac{p(x, y=0, z, \lambda_{ex}=532 \text{ nm})}{p(x, y=0, z, \lambda_{ex}=658 \text{ nm})}, \frac{p(x, y=0, z, \lambda_{ex}=532 \text{ nm})}{p(x, y=0, z, \lambda_{ex}=1064 \text{ nm})}, \frac{p(x, y=0, z, \lambda_{ex}=658 \text{ nm})}{p(x, y=0, z, \lambda_{ex}=1064 \text{ nm})} \right)$ were calculated for simple geometries and all considered blood oxygen saturation values. The trends of the OA signal ratios vs blood oxygen saturation were monotonous, and the ratio

$$R(x, y, z) = \frac{p(x, y, z, \lambda_{ex}=658 \text{ nm})}{p(x, y, z, \lambda_{ex}=1064 \text{ nm})}, \quad (2)$$

revealed the smallest variation within all cases (vessel depth and location) for particular values of StO_2 . In this connection, the average value

$$\tilde{R} = \frac{\langle p(x, y=0, z, \lambda_{ex}=658 \text{ nm}) \rangle_{(x, y=0, z) \in ves}}{\langle p(x, y=0, z, \lambda_{ex}=1064 \text{ nm}) \rangle_{(x, y=0, z) \in ves}}, \quad (3)$$

where $\langle p(x, y = 0, z, \lambda_{ex}) \rangle_{(x, y=0, z) \in ves}$ means the OA signal in central cross-section of blood vessel corresponding to probing wavelength λ_{ex} averaged over all available cases, was employed to construct the mean dependence $\tilde{R}(\text{StO}_2)$. The inverse function $\widetilde{\text{StO}_2}(\tilde{R})$ was further employed for voxel-by-voxel estimation of blood oxygen saturation based on the calculated ratio $R(x, y = 0, z)$:

$$\text{StO}_2(x, y = 0, z) = \widetilde{\text{StO}_2}(R(x, y = 0, z)). \quad (4)$$

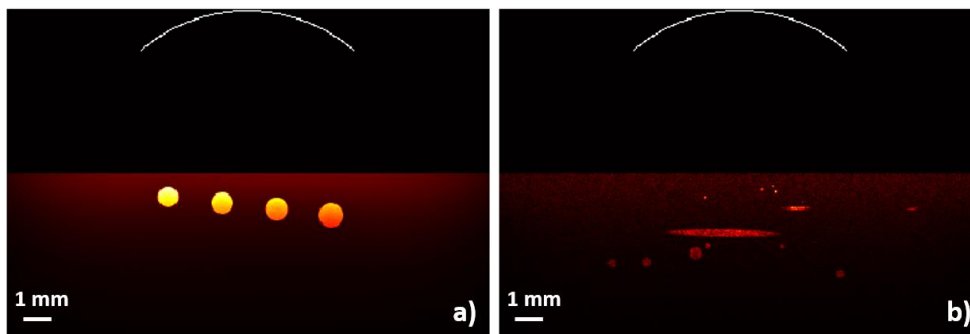


Fig. 3 Schematic of three-dimensional detector and initial pressure distribution obtained from MC modeling in projection to XZ-plane for vessel configuration from: a) Fig. 1c; b) Fig. 2b.

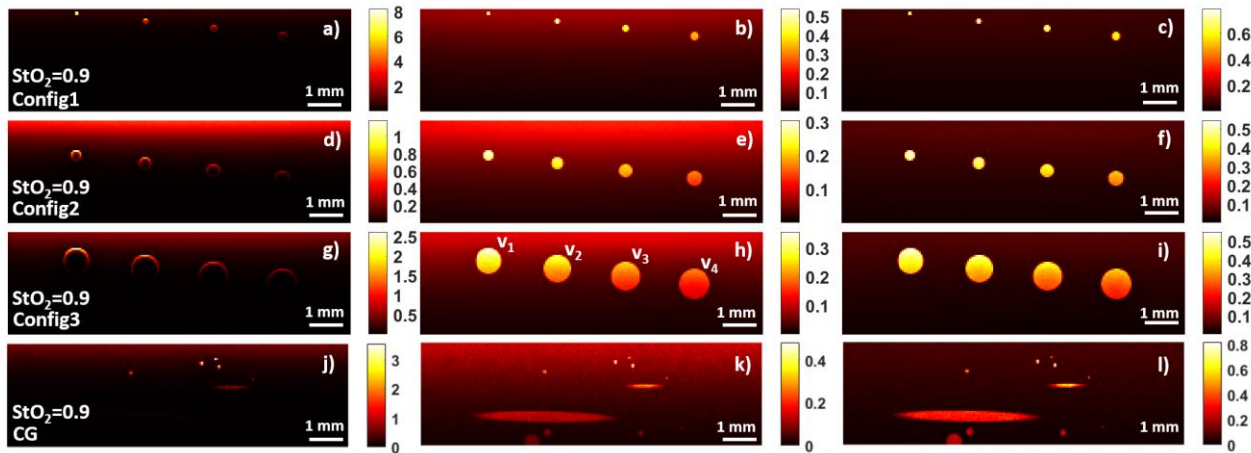


Fig. 4 Three-dimensional maps (side view, XZ-plane) of the distribution of absorbed light dose in XZ-plane $H(x, y = 0, z, \lambda_{ex})$ for probing wavelengths of $\lambda_{ex} = 532$ nm (a, d, g, j), $\lambda_{ex} = 658$ nm (b, e, h, k), and $\lambda_{ex} = 1064$ nm (c, f, i, l) and for configurations shown in Fig. 1 (Config1 – a, b, c; Config2 – d, e, f; Config3 – g, h, i) and 2D projection of complex geometry (CG) from Fig. 2b (j, k, l). Notations v1–v4 indicate vessels chosen for further detailed analysis.

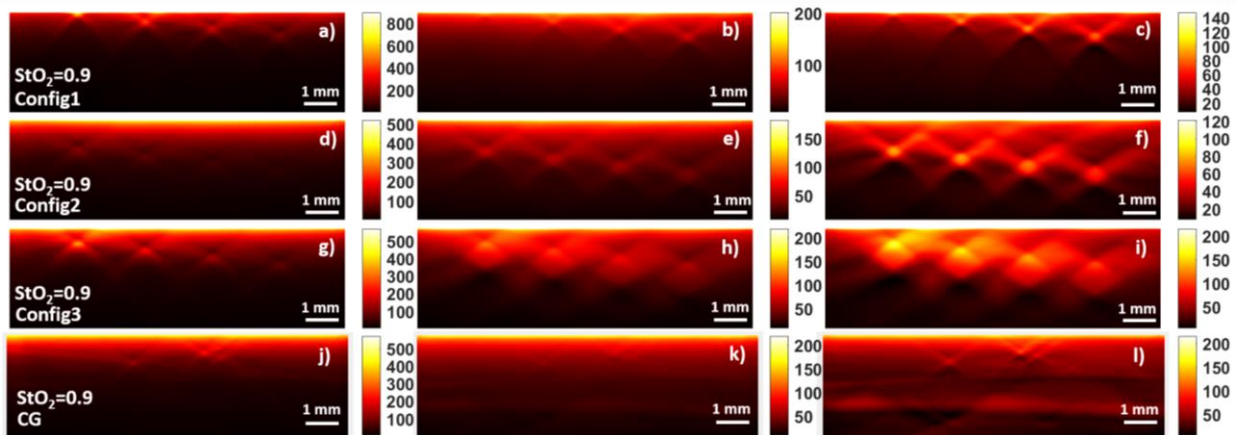


Fig. 5 Reconstructed OA B-scans $p(x, y = 0, z, \lambda_{ex})$ obtained from k-Wave modeling for probing wavelengths of $\lambda_{ex} = 532$ nm (a, d, g, j), $\lambda_{ex} = 658$ nm (b, e, h, k), and $\lambda_{ex} = 1064$ nm (c, f, i, l) and for configurations shown in Fig. 1 (Config1 – a, b, c; Config2 – d, e, f; Config3 – g, h, i) and 2D projection of complex geometry (CG) from Fig. 2b (j, k, l).

3 Results and Discussion

3.1 Monte Carlo Modeling

Fig. 4 shows central cross-sections of three-dimensional maps of absorbed light dose $H(x, y = 0, z, \lambda_{ex})$ in blood vessels for their various diameters and embedding depths for probing wavelengths of 532 nm (Fig. 4a), 658 nm (Fig. 4b) and 1064 nm (Fig. 4c) and three different configurations from Fig. 1 and 2D projection of complex geometry (Fig. 2b).

Absorption coefficient of blood for 532 nm is significantly higher than those for 658 nm or 1064 nm, which significantly limits the penetration of radiation of this wavelength into blood vessels, which is manifested by primary absorption of light on the boundaries of blood vessels (Fig. 4a), while for 658 nm and 1064 nm probing light is absorbed in the entire volume of vessels (Figs. 4b, c).

3.2 k-Wave Modeling of OA Images

At the second stage, based on the obtained absorption maps (Fig. 4), the acoustic response of the medium was calculated using the k-Wave Toolbox [39] and reconstructed by the earlier proposed algorithm [43] for all probing wavelengths. The results corresponding to configurations from Fig. 1 and Fig. 2b are shown in Fig. 5.

Due to limitations of RAM capacity of the employed workstation (although it is highest available for non-server solutions) the grid element size was chosen equal to 50 μm , which exceeds the scanning step in a real OA imaging system [42]; in addition, the central frequency of ultrasound detector is lower for numerical modelling as compared to the real system, which leads to the presence of artifacts in the reconstructed OA images.

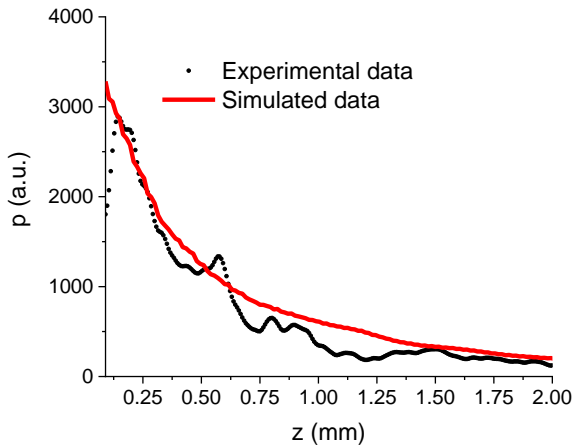


Fig. 6 Dependencies of average OA signals vs depth obtained *in vivo* [41] (Experimental data) and from k-Wave modeling (Simulated data).

Moreover, real OA systems operate with complicated illumination geometry (circular or through the center of the ultrasound detector [42, 44]), while this study is limited by a plane wave illumination case. These limitations lead to the presence of pronounced artifacts around the vessels location areas. In order to analyze the adequacy of the employed simulation approach we have compared the averaged A-scan (OA signal vs Z coordinate) for the experimental OA image of a human palm *in vivo* data [41] with the same dependence for a simulated image (Fig. 6). This comparison reveals good

agreement of OA signal attenuation, and the only discrepancy is observed in the top tissue layer, where simulated signal exceeds the experimental one. This discrepancy is explained by a simplified skin model employed in simulations, in which morphological skin layers are not distinguished, while in real skin upper stratum corneum and epidermis layers contain no blood thus producing weak OA signal. Nevertheless, good correspondence of the general trend allows concluding on the adequacy of the employed model given that proper normalization is done.

3.3 Reconstruction of Blood Oxygen Saturation from Ratio of Signal Intensities

Figs. 7a–c show the dependencies of OA signal intensities averaged over each of four blood vessels (denoted as v1–v4 in Fig. 4h) on blood oxygen saturation, which were obtained in numerical simulation. Figs. 7d–f shows the ratios of the signals registered at different probing wavelengths. It is worth mentioning that the signals show monotonous dependence on StO_2 owing to monotonous dependence of the medium optical properties on this parameter. However, they show different trends owing to difference in absorption spectra of oxy- and deoxyhemoglobin. The revealed monotonous dependence of signal ratio in this respect is more important, since it demonstrates the feasibility of employing the ratiometric approach in saturation reconstruction.

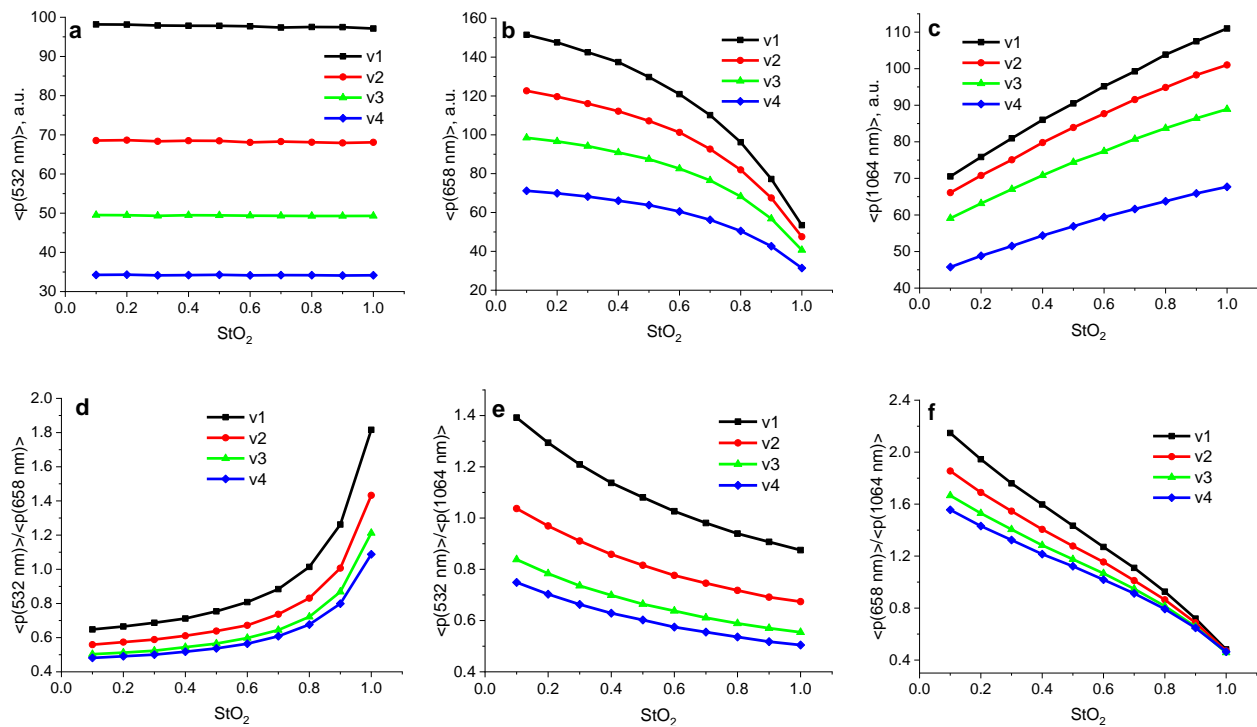


Fig. 7 Dependencies of OA signal intensity on blood oxygen saturation for probing depths of a) 532 nm, b) 658 nm, and c) 1064 nm and corresponding ratios: d) $\frac{p(x,y=0,z,\lambda_{ex}=532 nm)}{p(x,y=0,z,\lambda_{ex}=658 nm)}$, e) $\frac{p(x,y=0,z,\lambda_{ex}=532 nm)}{p(x,y=0,z,\lambda_{ex}=1064 nm)}$, f) $\frac{p(x,y=0,z,\lambda_{ex}=658 nm)}{p(x,y=0,z,\lambda_{ex}=1064 nm)}$. Notations v1–v4 indicate vessels in Fig. 4h from left to right.

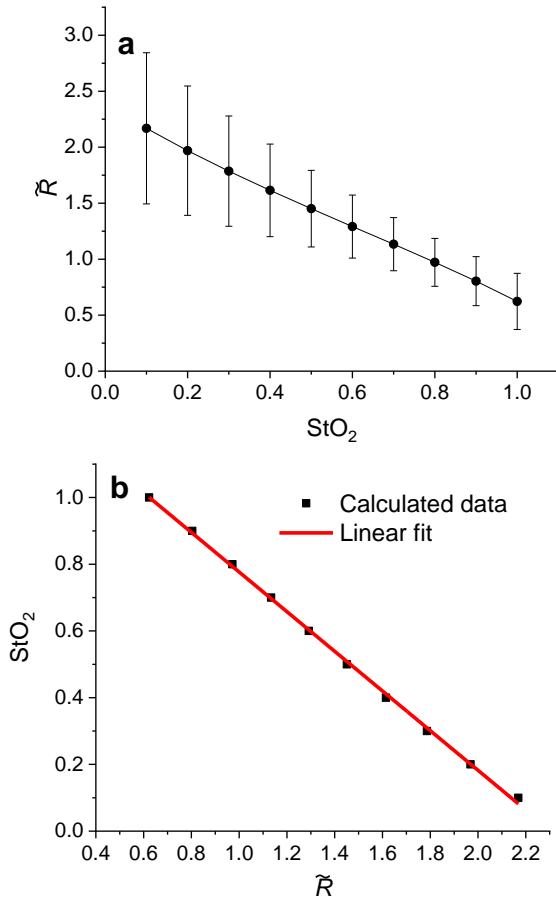


Fig. 8 (a) Mean dependence of OA signals ratio \tilde{R} vs blood oxygen saturation StO_2 calculated for all 50 simple geometry configurations; (b) inverse function $\widetilde{StO_2}(\tilde{R})$ and its approximation with linear fit.

The ratio of OA signals in central cross-section of blood vessels corresponding to probing wavelengths of 658 nm and 1064 nm revealed the smallest variance within all three ratios (Fig. 6d–f), thus, it was employed for the generation of synthetic curve $\widetilde{StO_2}(\tilde{R} = \frac{\langle p(x,y=0,z,\lambda_{ex}=658\text{ nm}) \rangle_{(x,y=0,z) \in ves}}{\langle p(x,y=0,z,\lambda_{ex}=1064\text{ nm}) \rangle_{(x,y=0,z) \in ves}})$. Fig. 8a shows mean dependence of ratio \tilde{R} vs blood oxygen saturation averaged over all fifty considered geometries of blood vessels, which could be considered as a generalized dependence that could be used in saturation map construction.

Fig. 8a shows that the variance of the signal ratio \tilde{R} decreases with the increase in blood oxygen saturation, hence, it is smaller for the blood oxygen saturation values > 0.8 , which allows considering the obtained dependence to be used in a simple algorithm of blood oxygenation map reconstruction. The linear fit of inverse function $\widetilde{StO_2}(\tilde{R})$ depicted in Fig. 8b was employed for voxel-by-voxel reconstruction of blood oxygen saturation map based on the map of OA signal ratios ($R(x, y = 0, z) = \frac{p(x,y=0,z,\lambda_{ex}=658\text{ nm})}{p(x,y=0,z,\lambda_{ex}=1064\text{ nm})}$) derived from simulations results.

Fitting was performed within Matlab Curve Fitting Toolbox and revealed that dependence $\widetilde{StO_2}(R)$ is described with the following Eq.:

$$\widetilde{StO_2}(R) = -0.59R + 1.37, \quad (5)$$

with high precision (coefficient of determination $r^2 = 0.9991$). Reconstructed saturation value $StO_{2,rec}$ was calculated voxel-by-voxel from corresponding values of R . For the cases of reconstructing $StO_{2,rec}$ value outside the physiological range, below 0 or above 1, they were assumed to be equal to 0 or 1, respectively.

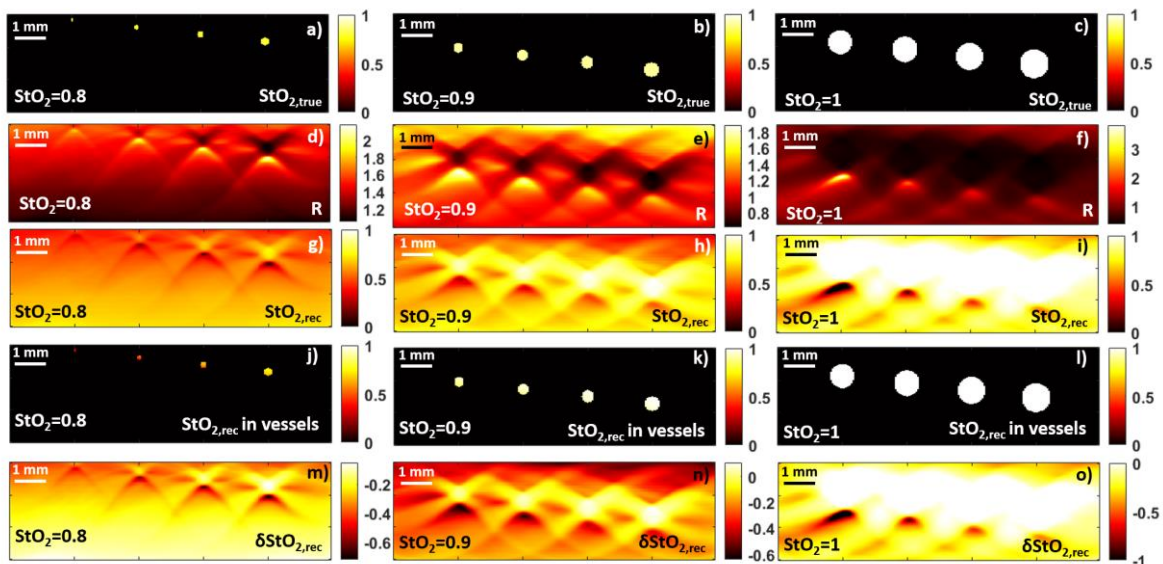


Fig. 9 Blood vessel configurations with $StO_{2,true}(x, y = 0, z)$ value (a, b, c), calculated ratio $R(x, y = 0, z)$ (d, e, f), reconstructed blood oxygen saturation $StO_{2,rec}(x, y = 0, z)$ (g, h, i), reconstructed blood oxygen saturation $StO_{2,rec}(x, y = 0, z)$ in vessels only (j, k, l) and the discrepancy of reconstructed blood oxygen saturation $\delta StO_{2,rec}(x, y = 0, z)$ (m, n, o) for initial blood oxygen saturation 0.8 (a, d, g, j, m), 0.9 (b, e, h, k, n), and 1 (c, f, i, l, o). Vessel configurations correspond to Fig. 1.

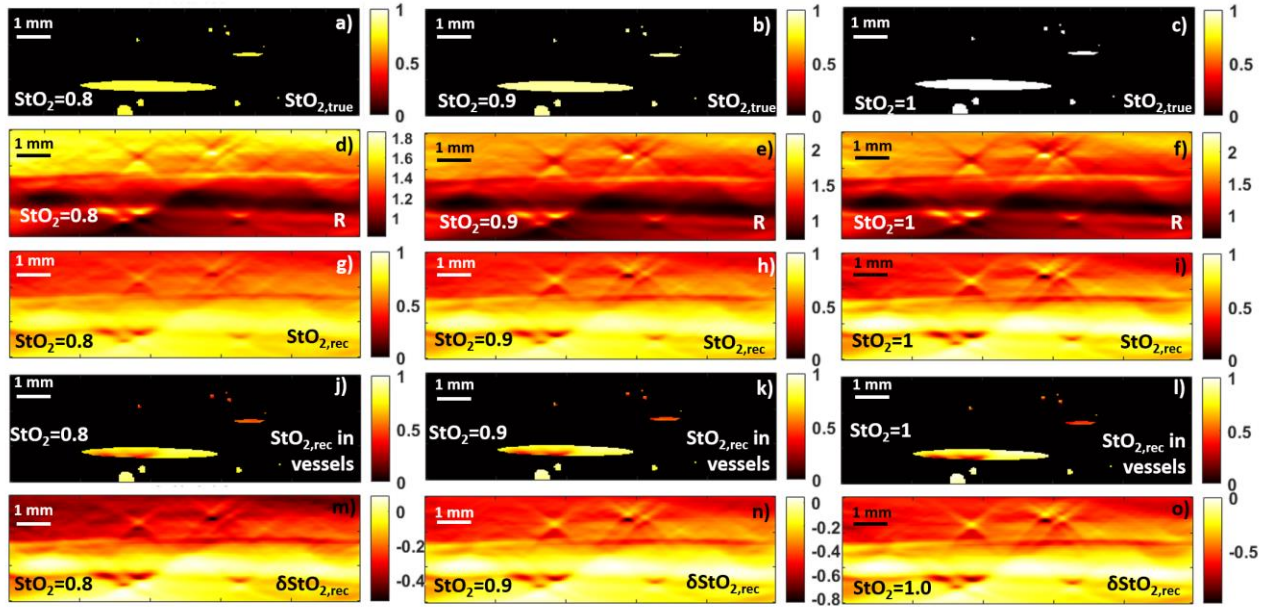


Fig. 10 Blood vessel configurations with $StO_{2,true}(x, y = 0, z)$ value (a, b, c), calculated ratio $R(x, y = 0, z)$ (d, e, f), reconstructed blood oxygen saturation $StO_{2,rec}(x, y = 0, z)$ (g, h, i), reconstructed blood oxygen saturation $StO_{2,rec}(x, y = 0, z)$ in vessels only (j, k, l) and the discrepancy of reconstructed blood oxygen saturation $\delta StO_{2,rec}(x, y = 0, z)$ (m, n, o) for initial blood oxygen saturation 0.8 (a, d, g, j, m), 0.9 (b, e, h, k, n) and 1 (c, f, i, l, o). Vessel configurations correspond to Fig. 2b.

The results of reconstruction for several simple geometry cases (shown in Fig. 1) are shown in Fig. 9, while the results for the complex geometry (Fig. 2b) are shown in Fig. 10. Each figure contains vessel location schematic, calculated XZ projections maps of OA signals ratio $R(x, y = 0, z)$, projections of full reconstructed maps of StO_2 and reconstructed StO_2 values in vessels only, and the discrepancy between reconstructed ($StO_{2,rec}$) and true ($StO_{2,true}$) (blood oxygen saturation values, calculated as:

$$\begin{aligned} \delta StO_{2,rec}(x, y = 0, z) &= \\ &= StO_{2,rec}(x, y = 0, z) - StO_{2,true}(x, y = 0, z). \end{aligned} \quad (6)$$

For the calculation of $\delta StO_{2,rec}$ the true blood oxygen saturation value in surrounding tissue outside the vessels was assumed equal to that in vessels, since the distribution of the light field generating OA signal is governed by absorption in vessels, although the considered signals originate from the nearby voxels.

As can be seen from Figs. 9–10, the proposed simple reconstruction algorithm provides with adequate estimation of blood oxygen saturation in vessels with no *a priori* knowledge of vessel embedding depth required. The discrepancy $\delta StO_{2,rec}$ between reconstructed and true blood oxygen saturation, $StO_{2,rec}$ and $StO_{2,true}$, is the highest for thin and subcutaneous vessels (Figs. 9–10). The ratio R is higher for subcutaneous vessels (Fig. 9d–f, Fig. 10d–f), which leads to smaller values of $StO_{2,rec}$ and, thus, to larger

discrepancy $\delta StO_{2,rec}$. For thick vessels $\delta StO_{2,rec}$ value increases with the increase in their embedding depth due to attenuation of probing light and corresponding decrease in OA signal. This effect is demonstrated in details in Fig. 11, which shows the dependencies of mean error in vessels on their diameter d and embedding depth z_0 calculated for all vessels in all considered simple geometry OA images (Fig. 1) calculated as mean discrepancy over all voxels belonging to a certain vessel:

$$\overline{\delta StO_{2,rec}} = \langle \delta StO_{2,rec}(x, y, z) \rangle_{ves}. \quad (7)$$

From Fig. 11 one can see that described effects lead to the presence of the minimal $\delta StO_{2,rec}$ (precision < 3%) area, which corresponds to the combinations of parameters that provide the mean values of the calibration curve $\tilde{R}(\overline{StO_2})$ (Fig. 8a) employed for the reconstruction algorithm. For the combination of vessel diameter d and embedding depth z_0 above that area the precision is < 15% for $StO_{2,true} \geq 0.8$. The reconstruction algorithm employs mean values of R , which correspond to the intermediate values of vessel embedding depth thus providing better accuracy for these depths (Fig. 11). For blood vessels located below those depths, the ratio R is smaller due to stronger attenuation of probing light at 658 nm compared to 1064 nm. This leads to overestimation of StO_2 and positive values of $\delta StO_{2,rec}$ (Fig. 11).

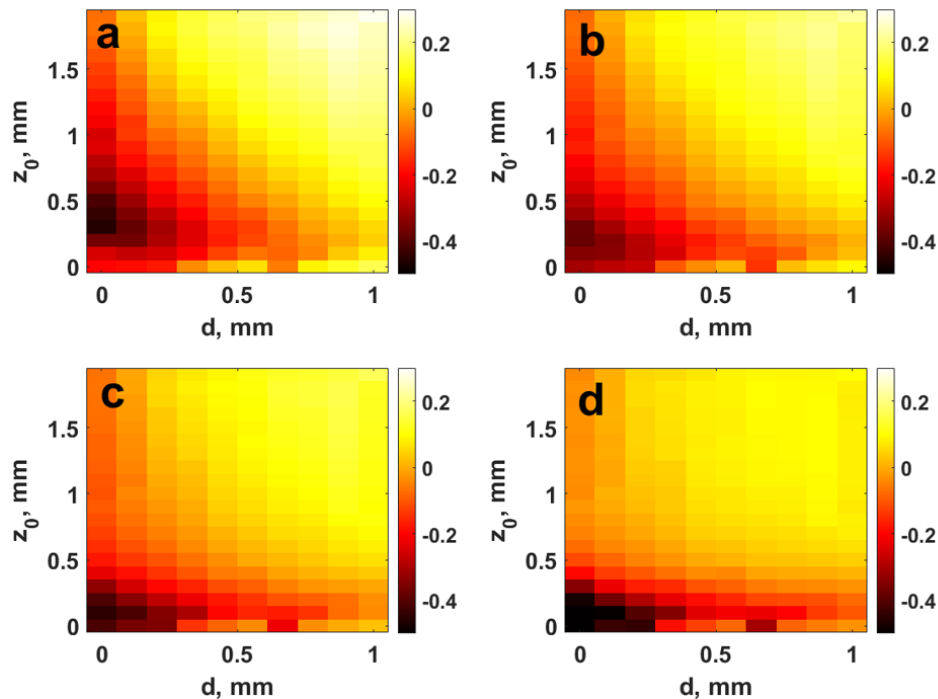


Fig. 11 Dependencies of discrepancy of blood oxygen saturation reconstruction $\delta\text{StO}_{2,\text{rec}}$ in vessels on their diameter d and embedding depth z_0 for blood oxygen saturation value of (a) 0.6, (b) 0.7, (c) 0.8, and (d) 0.9 calculated for all considered vessels in simple geometry.

On the contrary, the algorithm reveals underestimation of StO_2 for subcutaneous vessels. For estimating saturation at minimal and maximal depths among all considered values z_0 it is reasonable to account for the value of z_0 in the reconstruction algorithm for a more precise estimation of StO_2 .

It should also be noted that the values of ratio R are comparable for blood vessels and reconstruction artifacts (Figs. 9–10), which may lead to uncertainties in interpreting the constructed maps. The employment of illumination geometries of real OA systems and three-dimensional reconstruction instead of simplified planar wave case considered in this study has potential to eliminate the reconstruction artifacts and provide with more precise estimation of oxygen saturation in surrounding tissues as well as in blood vessels, however, it requires larger computational power.

4 Conclusion

In this study, a set of OA images of biotissue with embedded vessels was numerically simulated for different orientations, diameters, embedding depths and blood oxygen saturation of vessels. Numerical simulations are based on sequential employment of developed MC algorithm and k-Wave Toolbox. The ratio of averaged OA signals corresponding to different probing wavelengths revealed monotonous dependence on blood oxygen saturation for different pairs of the wavelengths of 532, 680, and 1064 nm. The dependence of ratio R of OA signals corresponding to probing wavelengths of 658 nm and 1064 nm on blood oxygen saturation demonstrated the smallest variance for all

diameters and depths of vessels and was employed for a simple estimation of StO_2 value. The algorithm was based on the construction of inverse function $\widetilde{\text{StO}}_2(R)$ and voxel-by-voxel estimation of blood oxygen saturation value based on the calculated ratio R . Proposed algorithm was tested on simulated OA images for simple and complex vessel geometry. In the space of vessel diameters and embedding depths for a given true value of blood oxygen saturation there is an area of vessel diameters d and embedding depths z_0 that are closed for the values contributing to the average ratio dependence, which provides the reconstruction accuracy better than 3%. For the combination of vessel diameter d and embedding depth z_0 above that area the precision is below 15% for true StO_2 values ≥ 0.8 . Three-dimensional OA reconstruction employed instead of 2-dimensional modality considered in this study has potential to improve the algorithm performance, since it allows eliminating artifacts from OA images. Moreover, depth-dependent StO_2 reconstruction is expected to provide even higher accuracy. In this connection, employing a more advanced, however, time-consuming approach to OA image simulations in combination with machine learning techniques instead of the considered simple algorithm has high potential in accurate mapping of blood oxygenation based on spectral OA data.

Disclosures

The authors declare no conflict of interest.

Acknowledgements

The study is supported by Russian Science Foundation (project #22-29-00074).

References

1. C. Menon, D. L. Fraker, “[Tumor oxygenation status as a prognostic marker](#),” *Cancer Letters* 221(2), 225–235 (2005).
2. C. Zhou, R. Choe, N. S. Shah, T. Durduran, G. Yu, A. Durkin, D. Hsiang, R. Mehta, J. A. Butler, and A. E. Cerussi, “[Diffuse optical monitoring of blood flow and oxygenation in human breast cancer during early stages of neoadjuvant chemotherapy](#),” *Journal of Biomedical Optics* 12(5), 051903 (2007).
3. A. A. Tandara, T. A. Mustoe, “[Oxygen in wound healing—more than a nutrient](#),” *World Journal of Surgery* 28, 294–300 (2004).
4. A. Orlova, Y. Perevalova, K. Pavlova, N. Orlinskaya, A. Khilov, D. Kurakina, M. Shakhova, M. Kleshnin, E. Sergeeva, and I. Turchin, “[In Diffuse optical spectroscopy monitoring of experimental tumor oxygenation after red and blue light photodynamic therapy](#),” *Photonics* 9(1), 19 (2022).
5. C. Balas, “[Review of biomedical optical imaging—a powerful, non-invasive, non-ionizing technology for improving in vivo diagnosis](#),” *Measurement Science and Technology* 20(10), 104020 (2009).
6. A. P. Dhawan, B. D’Alessandro, and X. Fu, “[Optical imaging modalities for biomedical applications](#),” *IEEE Reviews in Biomedical Engineering* 3, 69–92 (2010).
7. T. Durduran, G. Yu, M. G. Burnett, J. A. Detre, J. H. Greenberg, J. Wang, C. Zhou, and A. G. Yodh, “[Diffuse optical measurement of blood flow, blood oxygenation, and metabolism in a human brain during sensorimotor cortex activation](#),” *Optics Letters* 29(15), 1766–1768 (2004).
8. S. E. Boebinger, R. O. Brothers, S. Bong, B. Sanders, C. McCracken, L. H. Ting, and E. M. Buckley, “[Diffuse optical spectroscopy assessment of resting oxygen metabolism in the leg musculature](#),” *Metabolites* 11(8), 496 (2021).
9. D. Kurakina, V. Perekatova, E. Sergeeva, A. Kostyuk, I. Turchin, and M. Kirillin, “[Probing depth in diffuse reflectance spectroscopy of biotissues: A monte carlo study](#),” *Laser Physics Letters* 19, 035602 (2022).
10. A. Orlova, M. Y. Kirillin, A. Volovetsky, N. Y. Shilyagina, and E. Sergeeva, G. Y. Golubiatnikov, and I. Turchin, “[Diffuse optical spectroscopy monitoring of oxygen state and hemoglobin concentration during skbr-3 tumor model growth](#),” *Laser Physics Letters* 14, 015601 (2016).
11. A. F. Khan, F. Zhang, H. Yuan, and L. Ding, “[Brain-wide functional diffuse optical tomography of resting state networks](#),” *Journal of Neural Engineering* 18, 046069 (2021).
12. J. P. Culver, T. Durduran, D. Furuya, C. Cheung, J. H. Greenberg, and A. Yodh, “[Diffuse optical tomography of cerebral blood flow, oxygenation, and metabolism in rat during focal ischemia](#),” *Journal of Cerebral Blood Flow & Metabolism* 23(8), 911–924 (2003).
13. L. D. Liao, M. L. Li, H. Y. Lai, Y. Y. I. Shih, Y. C. Lo, S. Tsang, P. C. P. Chao, C. T. Lin, F. S. Jaw, and Y. Y. Chen, “[Imaging brain hemodynamic changes during rat forepaw electrical stimulation using functional photoacoustic microscopy](#),” *Neuroimage* 52(2), 562–570 (2010).
14. E. Liapis, A. Karlas, U. Klemm, and V. Ntziachristos, “[Chemotherapeutic effects on breast tumor hemodynamics revealed by eigenspectra multispectral optoacoustic tomography \(emsot\)](#),” *Theranostics* 11(16), 7813 (2021).
15. A. Orlova, M. Sirotkina, E. Smolina, V. Elagin, A. Kovalchuk, I. Turchin, and P. Subochev, “[Raster-scan optoacoustic angiography of blood vessel development in colon cancer models](#),” *Photoacoustics* 13, 25–32 (2019).
16. P. Subochev, E. Smolina, E. Sergeeva, M. Kirillin, A. Orlova, D. Kurakina, D. Emyanov, and D. Razansky, “[Toward whole-brain in vivo optoacoustic angiography of rodents: Modeling and experimental observations](#),” *Biomedical Optics Express* 11(3), 1477–1488 (2020).
17. L. V. Wang, “[Multiscale photoacoustic microscopy and computed tomography](#),” *Nature Photonics* 3, 503–509 (2009).
18. L. V. Wang, S. Hu, “[Photoacoustic tomography: In vivo imaging from organelles to organs](#),” *Science* 335, 1458–1462 (2012).
19. X. L. Deán-Ben, D. Razansky, “[Optoacoustic imaging of the skin](#),” *Experimental Dermatology* 30, 1598–1609 (2021).
20. V. Perekatova, P. Subochev, M. Y. Kirillin, E. Sergeeva, D. Kurakina, A. Orlova, A. Postnikova, and I. Turchin, “[Quantitative techniques for extraction of blood oxygenation from multispectral optoacoustic measurements](#),” *Laser Physics Letters* 16, 116201 (2019).
21. M. Schwarz, A. Buehler, J. Aguirre, and V. Ntziachristos, “[Three-dimensional multispectral optoacoustic mesoscopy reveals melanin and blood oxygenation in human skin in vivo](#),” *Journal of Biophotonics* 9, 55–60 (2016).
22. M. Kirillin, V. Perekatova, I. Turchin, and P. Subochev, “[Fluence compensation in raster-scan optoacoustic angiography](#),” *Photoacoustics* 8, 59–67 (2017).

23. J. Gröhl, M. Schellenberg, K. Dreher, and L. Maier-Hein, “[Deep learning for biomedical photoacoustic imaging: A review](#),” *Photoacoustics* 22, 100241 (2021).
24. H. Deng, H. Qiao, Q. Dai, and C. Ma, “[Deep learning in photoacoustic imaging: A review](#),” *Journal of Biomedical Optics* 26(4), 040901 (2021).
25. C. Yang, H. Lan, F. Gao, and F. Gao, “[Review of deep learning for photoacoustic imaging](#),” *Photoacoustics* 21, 100215 (2021).
26. J. Gröhl, T. Kirchner, T. J. Adler, L. Hacker, N. Holzwarth, A. Hernández-Aguilera, M. A. Herrera, E. Santos, S. E. Bohndiek, and L. Maier-Hein, “[Learned spectral decoloring enables photoacoustic oximetry](#),” *Scientific Reports* 11, 6565 (2021).
27. J. H. Nölke, T. Adler, J. Gröhl, T. Kirchner, L. Ardizzone, C. Rother, U. Köthe, and L. Maier-Hein, “[Invertible neural networks for uncertainty quantification in photoacoustic imaging](#),” *Bildverarbeitung Für Die Medizin* 2021, 330–335 (2021).
28. C. Yang, F. Gao, “[EDA-Net: Dense aggregation of deep and shallow information achieves quantitative photoacoustic blood oxygenation imaging deep in human breast](#),” in *International Conference on Medical Image Computing and Computer-Assisted Intervention*, Springer, Cham, 246–254 (2019).
29. K. Hoffer-Hawlik, G. P. Luke, “[Abso2luteu-net: Tissue oxygenation calculation using photoacoustic imaging and convolutional neural networks](#),” *ENGS 88 Honors Thesis* (2019).
30. G. P. Luke, K. Hoffer-Hawlik, A. C. Van Namen, and R. Shang, “[O-net: A convolutional neural network for quantitative photoacoustic image segmentation and oximetry](#),” *arXiv Preprint*, 1911.01935 (2019).
31. C. Bench, A. Hauptmann, and B. T. Cox, “[Toward accurate quantitative photoacoustic imaging: Learning vascular blood oxygen saturation in three dimensions](#),” *Journal of Biomedical Optics* 25(8), 085003 (2020).
32. L. Wang, S. L. Jacques, and L. Zheng, “[Mcm1—monte carlo modeling of light transport in multi-layered tissues](#),” *Computer Methods and Programs in Biomedicine* 47(2), 131–146 (1995).
33. M. Kirillin, A. Khilov, D. Kurakina, A. Orlova, V. Perekatova, V. Shishkova, A. Malygina, A. Mironycheva, I. Shlivko, S. Gamayunov, I. Turchin, and E. Sergeeva, “[Dual-wavelength fluorescence monitoring of photodynamic therapy: From analytical models to clinical studies](#),” *Cancers* 13(22), 5807 (2021).
34. A. V. Gorshkov, M. Y. Kirillin, “[Acceleration of monte carlo simulation of photon migration in complex heterogeneous media using intel many-integrated core architecture](#),” *Journal of Biomedical Optics* 20(8), 085002 (2015).
35. V. Perekatova, S. Nemirova, A. Orlova, M. Kirillin, A. Kurnikov, K. Pavlova, A. Khilov, A. Kovalchuk, and P. Subochev, “[Three-dimensional dual-wavelength optoacoustic angiography reveals arteriovenous anastomoses](#),” *Laser Physics Letters* 18, 045601 (2021).
36. V. Perekatova, P. Subochev, M. Kleshnin, and I. Turchin, “[Optimal wavelengths for optoacoustic measurements of blood oxygen saturation in biological tissues](#),” *Biomedical Optics Express* 7(10), 3979–3995 (2016).
37. N. Bosschaart, G. J. Edelman, M. C. Aalders, T. G. van Leeuwen, and D. J. Faber, “[A literature review and novel theoretical approach on the optical properties of whole blood](#),” *Lasers in Medical Science* 29, 453–479 (2014).
38. T. Kono, J. Yamada, “[In vivo measurement of optical properties of human skin for 450–800 nm and 950–1600 nm wavelengths](#),” *International Journal of Thermophysics* 40, 51 (2019).
39. B. E. Treeby, B. T. Cox, “[K-wave: Matlab toolbox for the simulation and reconstruction of photoacoustic wave fields](#),” *Journal of Biomedical Optics* 15(2), 021314 (2010).
40. I. Turchin, S. Bano, M. Kirillin, A. Orlova, V. Perekatova, V. Plekhanov, E. Sergeeva, D. Kurakina, A. Khilov, A. Kurnikov, P. Subochev, M. Shirmanova, A. Komarova, D. Yuzhakova, A. Gavrina, S. Mallidi, and T. Hasan, “[Combined fluorescence and optoacoustic imaging for monitoring treatments against ct26 tumors with photoactivatable liposomes](#),” *Cancers* 14(1), 197 (2021).
41. V. Perekatova, M. Kirillin, S. Nemirova, A. Orlova, A. Kurnikov, A. Khilov, K. Pavlova, V. Kazakov, V. Vildanov, I. Turchin, and P. Subochev, “[Quantitative characterization of age-related changes in peripheral vessels of a human palm using raster-scan optoacoustic angiography](#),” *Photonics* 9(7), 482 (2022).
42. P. Subochev, “[Cost-effective imaging of optoacoustic pressure, ultrasonic scattering, and optical diffuse reflectance with improved resolution and speed](#),” *Optics Letters* 41(5), 1006–1009 (2016).
43. V. V. Perekatova, M. Y. Kirillin, I. V. Turchin, and P. V. Subochev, “[Combination of virtual point detector concept and fluence compensation in acoustic resolution photoacoustic microscopy](#),” *Journal of Biomedical Optics* 23(9), 091414 (2018).
44. V. Perekatova, M. Kirillin, P. Subochev, A. Kurnikov, A. Khilov, A. Orlova, D. Yuzhakova, and I. Turchin, “[Quantification of microvasculature parameters based on optoacoustic angiography data](#),” *Laser Physics Letters* 18, 035602 (2021).